HITUBES PROJECT

DESIGN AND INTEGRITY ASSESSMENT OF HIGH STRENGTH TUBULAR STRUCTURES FOR EXTREME LOADING CONDITIONS

Deliverables 6.1, 6.2 & 6.3

D6.1: S-N data relevant to connections and refinement of the component method for bolted connections
D6.2: Simulations data on tubular members
D6.3: Simulation data on case studies and similar structural types.

Authors

Giuseppe Demofonti, Giuliana Zilli, Gian Marco Tamponi, Jan Ferino
Jean-Pierre Jaspart, Jean-François Demonceau, Long Van Hoang, Ly Dong Phuong Lam
Spyros Karamanos , Philip Perdikaris, Aglaia Pournara, Charis Papatheocharis, George Varelis
Oreste S. Bursi, Anil Kumar

Contributing Partners

Centro Sviluppo Materiali, Italy
Université de Liège, Belgium
University of Thessaly, Greece
University of Trento, Italy

Table of Contents

D.6.1. Determination of S-N data for welded and bolted relevant to connections and refinement of the component method

The design of welded tubular connections can be conducted either with the "classification of details" method, as described in EN 1993-1-9 [1], section 8 (referring to a limited number of joint geometries), or with the "hot spot stress" method. It has been widely recognized that the use of the former method (classification of details) is rather inappropriate for the fatigue design of welded tubular connections. It is noticed that EN 1993-1-9 covers only a small range of possible joint geometries. On the other hand, the latter method (hot spot stress) is by far the most efficient method for the fatigue design of such joints.

The hot spot method requires the calculation of the hot spot stress method, which is the maximum geometric stress at the vicinity of the weld. Subsequently, the fatigue design life is calculated though an appropriate fatigue S-N curve. The CIDECT guidelines [2] present a complete procedure for hot spot stress fatigue design, and propose a concise methodology for the calculation of the hot spot stress at a specific welded tubular joint, either though special-purpose parametric equations for stress concentration factors (SCF) or a finite element analysis. Furthermore, they propose a fatigue curve, expressed as follows:

$$\log\left(\mathrm{N_f}\right)=\frac{12.476-3\cdot\log\left(\mathrm{S_{rhs}}\right)}{1-0.18\cdot\log\left(\dfrac{16}{\mathrm{t}}\right)},\ \text{for } 10^3<\mathrm{N_f}<5\cdot10^6$$

$$\log\left(\mathrm{N_f}\right)=16.327-5\cdot\log\left(\mathrm{S_{rhs}}\right)+2.01\cdot\log\left(\frac{16}{\mathrm{t}}\right),\ \text{for } 5\cdot10^6<\mathrm{N_f}<10^8$$

The above fatigue curve is applicable for high-cycle fatigue, i.e. for number of cycles greater than 1,000. In addition, all fatigue curves available in various specifications refer to high-cycle fatigue, whereas there is a lack of provisions for low-cycle fatigue design, where the structural component is loaded with repeated excursions well into the inelastic rage of material behavior. One simple way to extend the high-cycle fatigue curves to the low-cycle regime has been proposed by Ballio et al. [3], where an "equivalent elastic stress range" is introduced and a linear extension of the S-N curves in the log-log scale is proposed. Using this approach, the predicted number of cycles for the X-joints under consideration under out-of-plane bending is equal to $N_{\mathbf{f}}=69$, whereas the corresponding experimental results for the two tested joints are equal to 240 and 200 cycles for weld conditions A and B respectively (the weld metal of weld A has a lower ultimate strength). Furthermore, the predicted number of cycles for the same X-joints under in-plane bending is equal to $N_{\mathbf{f}}=128$, whereas the experimental results are equal to 976 and 669 cycles for weld conditions A and B respectively, as reported earlier [4].

In Fig. 1.1 and Fig. 1.2, the experimental results are plotted in a fatigue graph together with the design fatigue curve proposed by CIDECT 8. In the same graph the linear extension of the proposed curve in the low-cycle-fatigue range is presented with dashed line type.

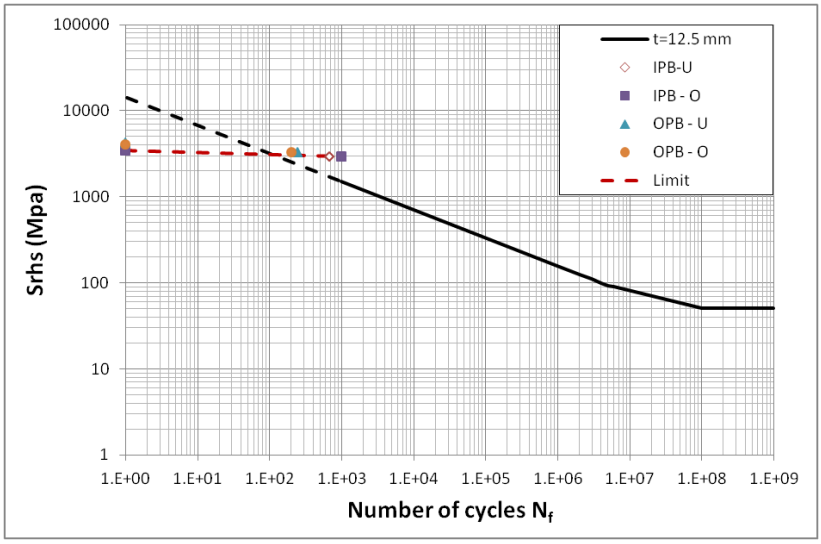

Figure1.1: Hot-spot-stress method fatigue curve and experimental data

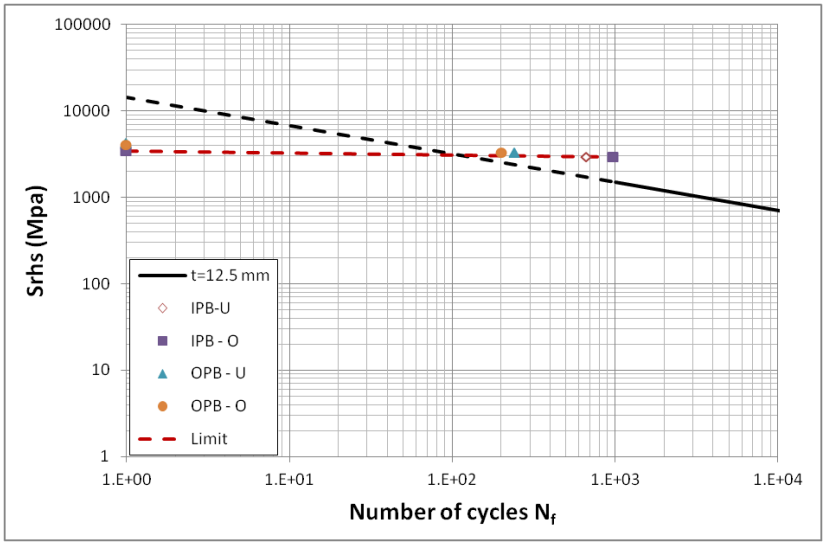

Figure 1.2: Fatigue curve and test data in the low-cycle regime.

The above shows that the "equivalent elastic stress range" methodology provides reasonable, yet conservative predictions for the fatigue life of the specimens, compared with the experimental fatigue life for a number of cycles not less than 100. Taking into consideration the inherited safety margins in the design specifications, it can be concluded that the use of this design methodology in the low-cycle fatigue range for a number of cycles not less than 100 results in safe predictions and can be adopted for design purposes [4].

The experimental results from monotonic tests indicate that in the fatigue area of 100 cycles and less, a nearly horizontal cut-off limit for the hot-spot stress needs to be considered (as shown in Fig. 1.1 and 1.2). The development of such a curve at this very-low-cycle fatigue regime requires to be verified by more tests. In the absence of those tests, a proposal is presented in the development of design guidelines, in a subsequent section of the report.

D.6.1.1. References

[1] EN 1993-1-9. 2002. Eurocode 3: Design of steel structures – Part 1-9: Fatigue strength of steel structures, European Committee for Standardization

[2] *CIDECT Design Guide No. 8. 2001. Design Guide for Circular and Rectangular Hollow Section Welded Joints under Fatigue Loading.*

[3] Ballio, G., Castiglioni, C.A., 1995. A Unified Approach for the Design of Steel Structures under Low and/or High cycle Fatigue. *Journal of Construction Steel Research*, 34, pp. 75-101

[4] Varelis, G. E., et al. 2012. Structural performance of TS590 high-strength steel welded tubular joints under extreme bending loading. *ISTS 14*, London, United Kingdom

D.6.2 Simulations the behaviour of tubular members under strong repeated loading with FE codes

D.6.2.1 Simulation of beam-column behavior under monotonic loading

The simulation of the monotonic experiments conducted by CSM have been conducted by developing finite numerical models using the FE program ABAQUS, as presented in [1]. The 1.5m-long tubular members of section ∅193.7/10 (considered as C specimens) are simulated with four-node reduced-integration shell elements, which have shown to perform very well in nonlinear analysis problems involving large inelastic deformations of relatively thick-walled steel cylinders. Based on thickness measurements, the tubes have been assumed with uniform outer diameter equal to 194.05mm and uniform thickness equal to 10.06mm. The tubular model is assumed perfect and the stiff tube segments which connect the specimen ends to the machine hinges are simulated as rigid members using appropriate beam elements. The numerical analysis allows for the calculation of bending strength under several levels of axial load, in accordance with the experimental procedure; axial load is applied first up to a certain prescribed level and, subsequently, keeping the axial load constant, bending is applied through an arc-length continuation algorithm (Riks) until a maximum bending moment is reached. Upon buckling formation, bending load is continued in the post-buckling range to obtain the buckled shape and compare with the experiments. The finite element results are compared with the experimental ones in terms of interaction diagram and moment-rotation curve a shown in Fig. 2.1 and 2.2, respectively. The shape of the buckle for the specimen C under combined loading is shown in Fig. 2.3.

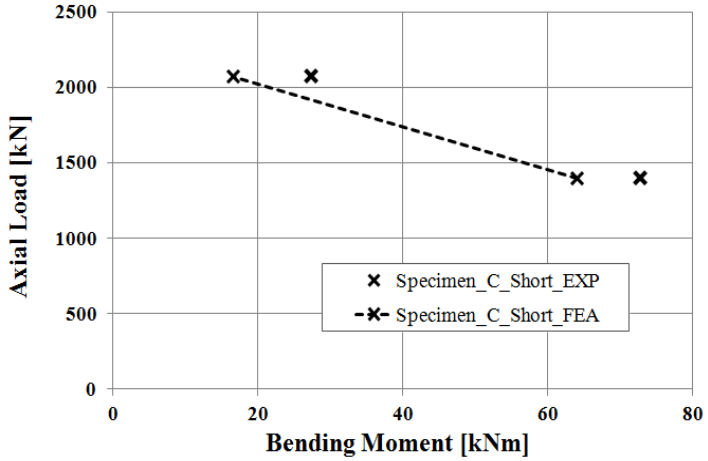

Figure 2.1: Finite element results in comparison with the experimental for 1.5m-long member of ∅193.7/10 section

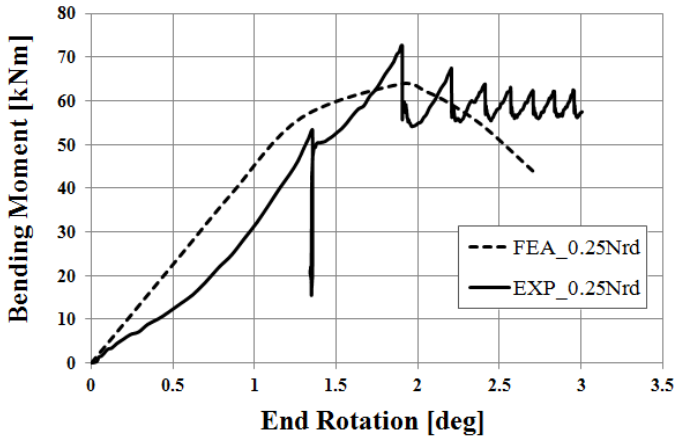

Figure 2.2: Finite element moment-end rotation curve (M-φ) in comparison with the experimental one for 1.5m-long member of ∅193.7/10 section

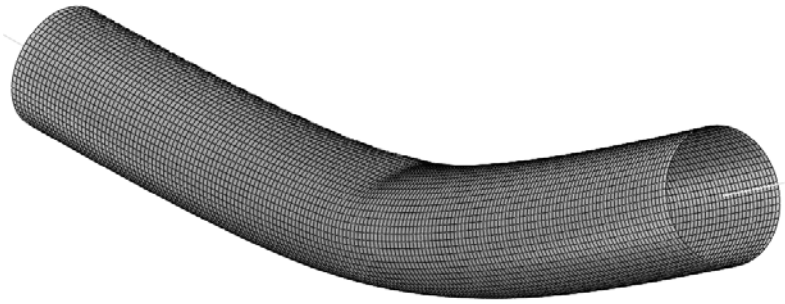

Figure 2.3: Failure mode of 1.5m-long member of ∅193.7/10 section under combined loading

D.6.2.2 Simulation of CHS member behavior under cyclic loading

For the simulation of the cyclic bending tests, detailed numerical models have been developed in ABAQUS FE code, as described in [2]. Each specimen was simulated using, 8-node solid (brick) elements with linear-hybrid formulation (C3D8H) adopting the mean measured geometrical characteristics measured before the bending tests started. The stiff beam-type members (referred to as "codolos") connecting both ends of the specimens with the hinges of the bending device were also modeled using linear beam-type elements (B31) and applying a properly selected profile section in order to take their flexibility into consideration. The connection between the specimen ends and the stiff beams was modeled assuming a kinematic coupling interaction of the end node of the stiff beam and the nodes on the perimeter of the cross-section at the specimen ends. A general view of the developed model for specimen type A is presented in Fig. 2.4. The loading protocol in each test was precisely the one that has been followed in the simulations. Cyclic bending of the specimens was introduced by controlling the end-rotations of the two stiff beams attached to each specimen.

The numerical predictions accuracy is highly depended on the capability of the adopted cyclic plasticity model to capture the cyclic plasticity phenomena (Bauschinger effect, ratcheting) and the change of the cross-sectional geometry (ovalization) that take place during the cyclic bending of the specimens. For the current simulations two plasticity models have been used, namely the von Mises plasticity model with linear kinematic hardening (LKH) and the Tseng – Lee model (TL) [3]. The latter is considered as a more advanced model which adopts the "bounding surface" concept and was implemented into ABAQUS through a user-subroutine (UMAT) developed for the purposes of the present project. The material model parameters have been properly calibrated based on the material testing results conducted by CSM.

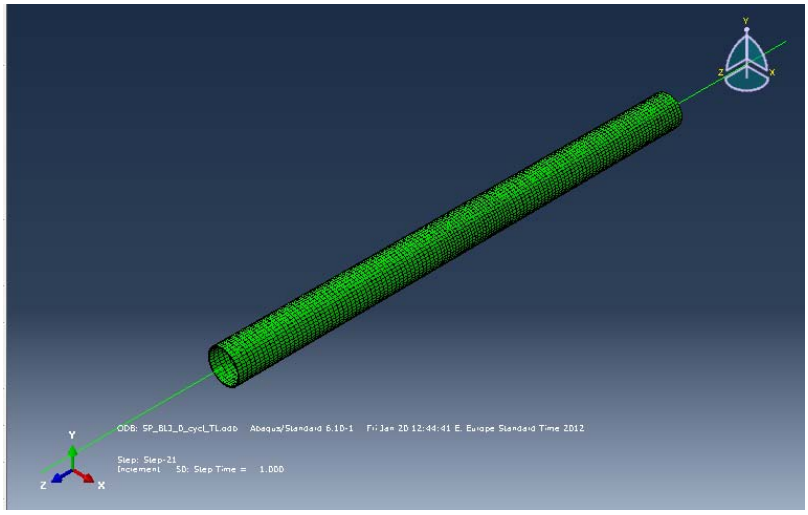

(a)

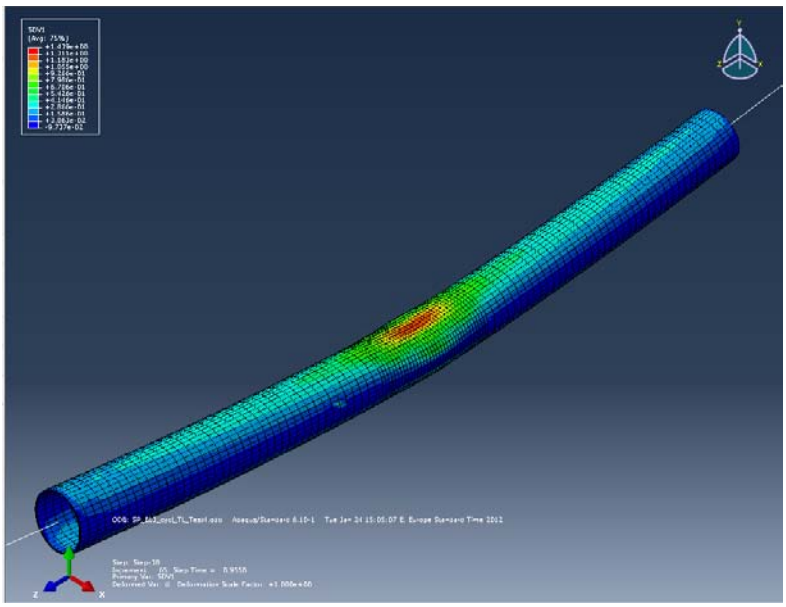

(b)

Figure 2.4: Finite element numerical model: (a) Undeformed shape, (b) Deformed shape.

The comparison between the experimental and numerical results for each test is presented in Fig.2.5-2.8. In addition, the evolution of flattening in two orthogonal directions of the cross-section and the ovalization are also reported for both models adopted (no test data have been available). The fitting between the experimental and the numerical load-displacement loops is considered satisfactory for the TL model. The LKH model overestimates the range of the elastic behavior of the tube under reverse bending, which is attributed to the fact that this model assumes a constant size of the yield surface throughout the analysis. Moreover, the evolution of flattening and ovalization according to the LKH model is also underestimated for the same reason compared to the predictions of the TL model.

The models also indicate significant accumulation of plastic deformation at the two ends of specimens of type A (Tests No.1 and No.3), which is responsible for cracking, i.e. the failure type observed in tests. On the other hand, for Tests No. 2 and No. 4 that resulted into buckling of the tested specimens, the numerical model with the TL model was able to predict the same failure mode in a slightly increased but very reasonable number of cycles. Generally, the observed differences near the two "corners" of the experimental loops are attributed to measurement acquisition issues and could be neglected. Moreover, the increased number of cycles required to cause buckling according to the numerical model compared with the experimental observations is to be expected since the buckling phenomenon is highly sensitive to the existence of initial imperfections, but such a sensitivity analysis is outside the scope of the present study.

The numerical model developed for the simulation of Test No. 2 has also been used for the examination of the member behavior under symmetric and on-symmetric moment-controlled cyclic bending in a moment level exceeding the elastic limit of the member. The specimen has been subjected to moment-controlled symmetric cyclic bending at ±730 KNm, a moment level which is able to cause plastic deformations on the member but it is lower than the maximum moment the member is able to sustain. The moment-rotation curves, the evolution of flattening and the ovalization evolution are presented in Fig. 2.9. The results indicate that due to the accumulation of plastic deformations and the evolution of the cross-section ovalization, there is a change of the resulting moment-rotation loops and a constant increase of the ovalization as the number of cycles increases. These are strong indications that after a sufficient number of cycles buckling of the specimen is probable to take place.

The case of non-symmetric moment-controlled cyclic bending has been also examined. The specimen under consideration has been subjected to moment-controlled non-symmetric cyclic bending at the level +730/-600 KNm. The resulting moment-rotation loops present a transition towards the higher load direction and the cross-sectional flattening and ovalization is constantly increasing (Fig. 2.10). Again, after a certain number of cycles, local buckling of the specimen is expected. The two observations

described above should be taken into consideration in order to introduce design guidelines for the tubular members under consideration.

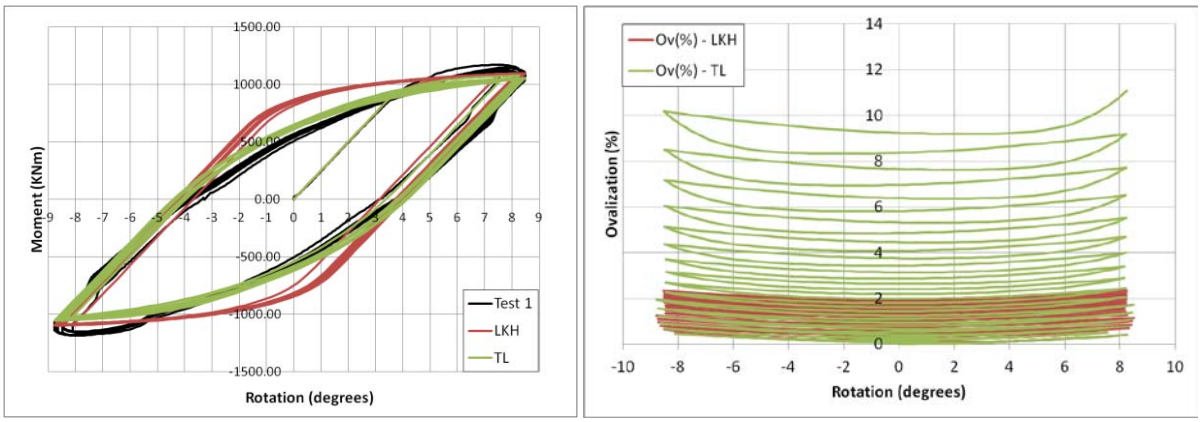

Figure 2.5: Test No. 1 – Cyclic moment-rotation curve; evolution of ovalization

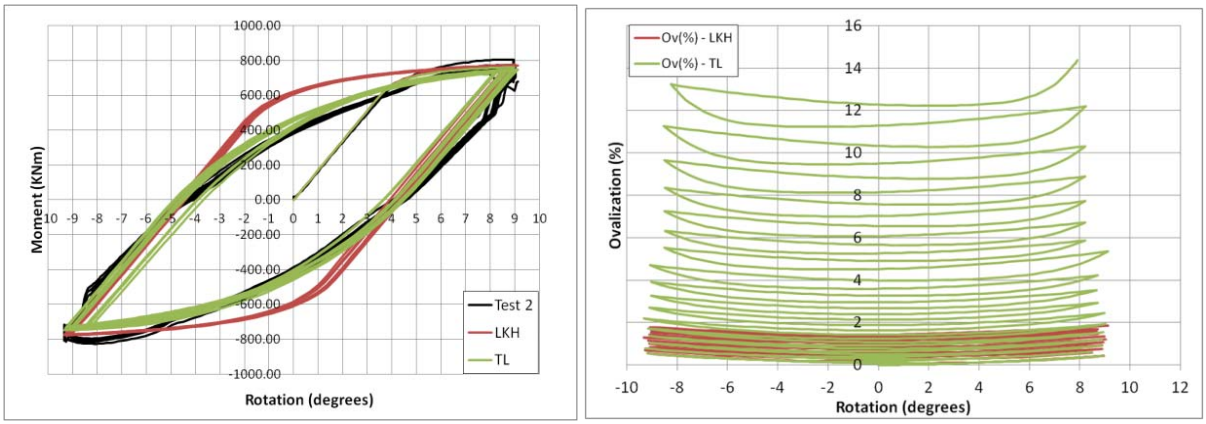

Figure 2.6: Test No. 2 – Cyclic moment-rotation curve; evolution of ovalization

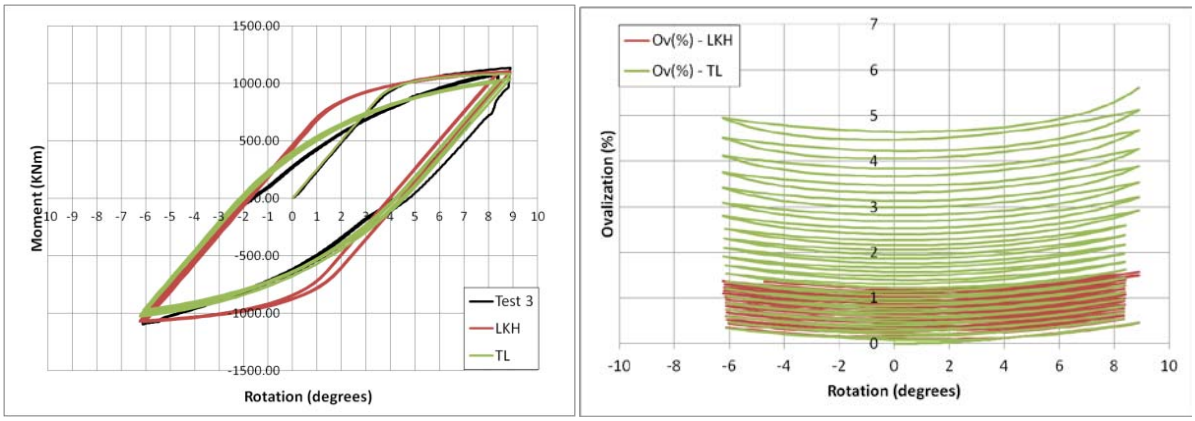

Figure 2.7: Test No. 3 – Cyclic moment-rotation curve; evolution of ovalization

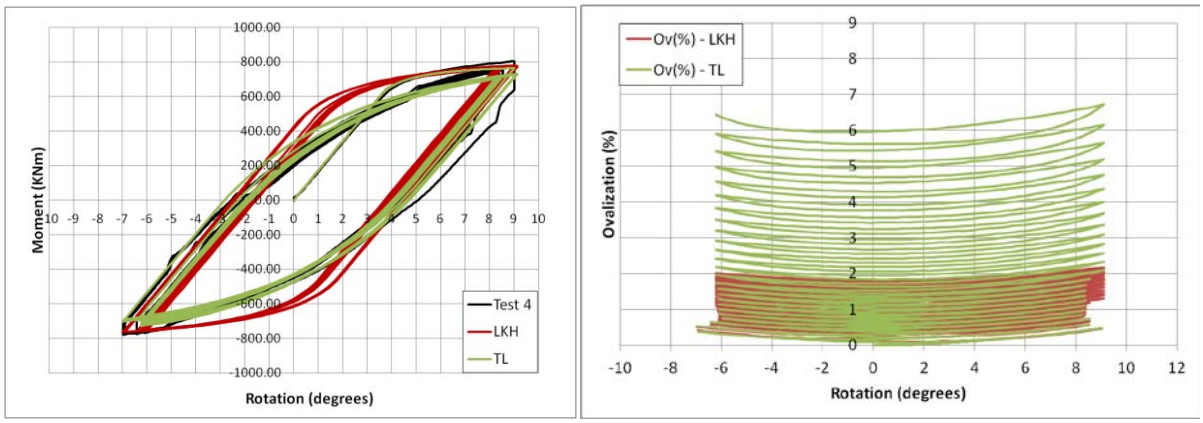

Figure 2.8: Test No. 4 – Cyclic moment-rotation curve; evolution of ovalization

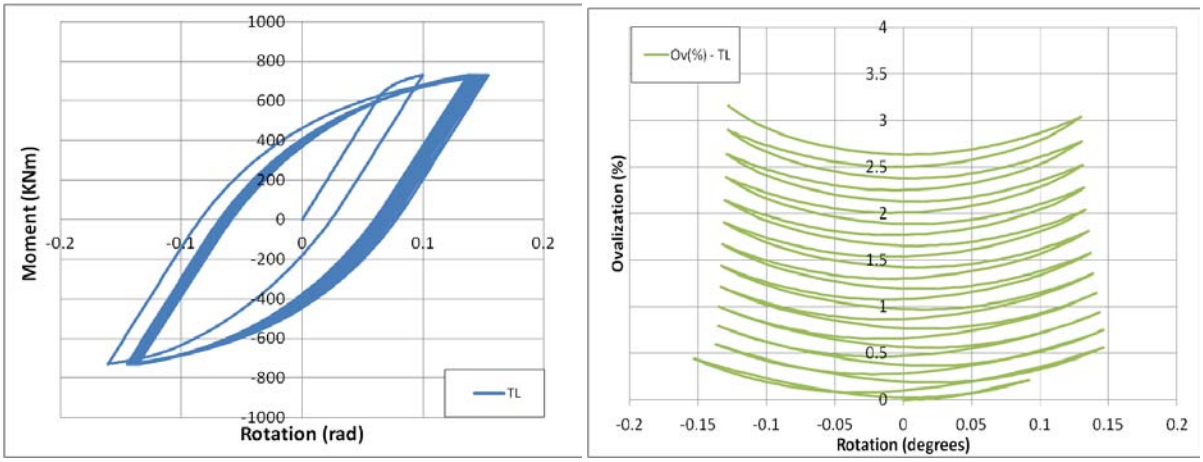

Figure 2.9: Moment-rotation curve and evolution of ovalization, for symmetric moment-controlled cyclic loading (section type B); numerical results.

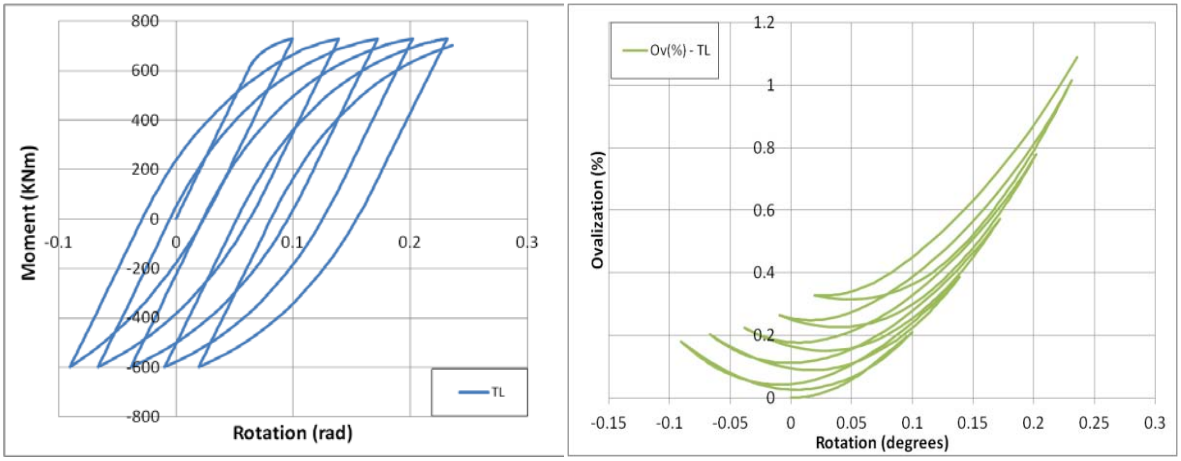

Figure 2.10: Moment-rotation curve and evolution of ovalization, for non-symmetric moment-controlled cyclic loading (section type B); numerical results.

D.6.2.3 References

[1] Aglaia-Eugenia Pournara and Spyros A. Karamanos, "Strength and Stability of High-Strength Steel Tubular Beam-Columns," *7th National Conference of Steel Structures*, Volos, Greece, September 2011.

[2] E. Varelis, Aglaia-Eugenia Pournara and Spyros A. Karamanos, "High-strength Steel Tubular Beam- Columns -Strength and Stability under Static and Cyclic Loading," *6th European Conference on Steel and Composite Structures*, Budapest, Hungary, September 2011.

[3] Tseng, N. T., Lee, G. C., (1983).” Simple plasticity model of the two-surface type”. ASCE, *J. of Engineering Mechanics* 109, 795-810.

D6.3: Simulation data on case studies and similar structural types - Deliverable D6.3

D.6.3.1 The Footbridge “Ponte del Mare”, Pescara, Italy

The main structure consists of two separated curved deck supported through stayed cables to a slightly inclined mast of height of about 50 m. The cycle deck has a length of 148m and a breadth of 4m whilst the pedestrian deck has a length of 167m and a breadth of 3m. The deck of the bridge is made of space truss members. The cross-section of the bridge-deck is made of open sections type L, HEA and HEB with regular carbon steel S 355 for cost savings. The supporting structure of the deck is coupled by means of a system of connection to the concrete floor of thickness of 10.5 cm that is put on a metal sheet of thickness 1 mm. The total weight of the steel of the bridge structure is 3848 kN. Relevant characteristics are shown in Figs. 3.1-3.3.

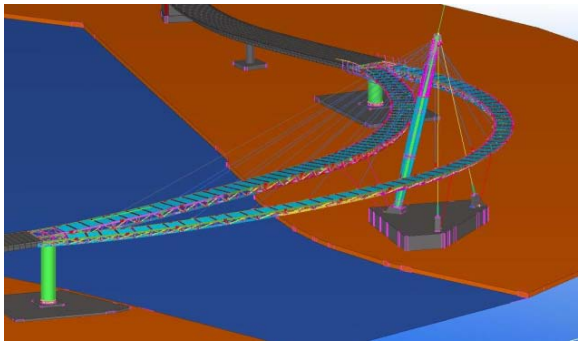

Fig. 3.1 Drawing of the footbridge “Ponte del Mare” of Pescara

Fig. 3.2 Footbridge “Ponte del Mare” in Pescara after construction

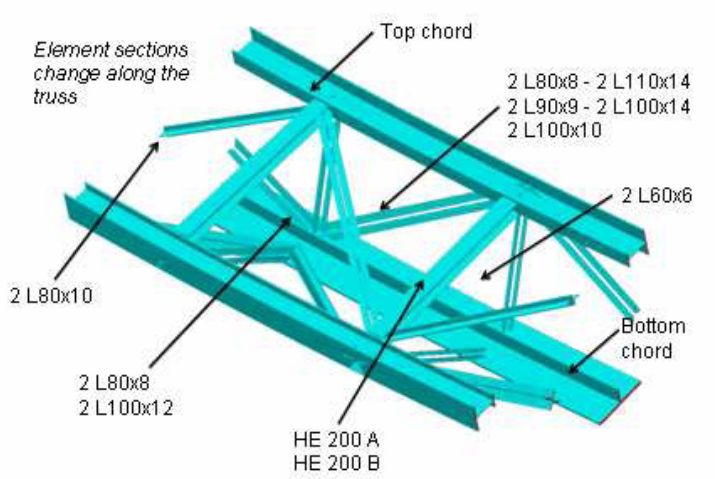

Fig. 3.3 Section of the Bridge Deck of "Ponte del Mare"

The modal analysis of the 'Ponte del Mare' footbridge gives the following modal frequencies.

Table 3.1 Modal frequencies of the structure without dampers

Mode	1	2	3	4	5	6	7	8	9	10	11
f[Hz]	0.68	1.00	1.09	1.14	1.37	1.52	1.55	1.67	1.70	1.98	2.13

The first ten mode shapes are depicted in the following figures A6.4a-j.

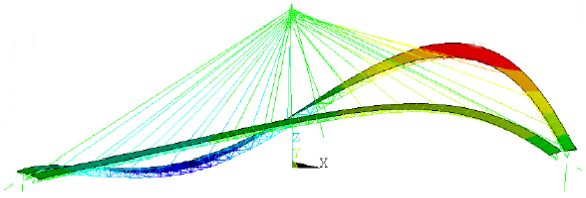

Fig. 3.4a 1st mode shape without dampers

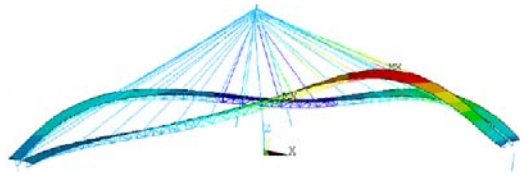

Fig. 3.4b 2nd mode shape without dampers

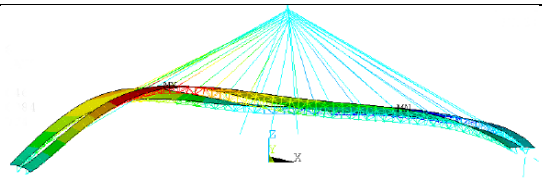

Fig. 3.4c 3rd mode shape without dampers

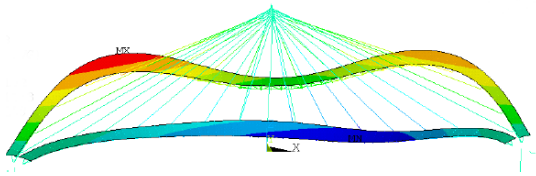

Fig. 3.4d 4th mode shape without dampers

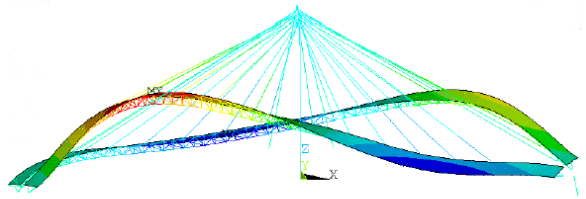

Fig. 3.4e 5th mode shape without dampers

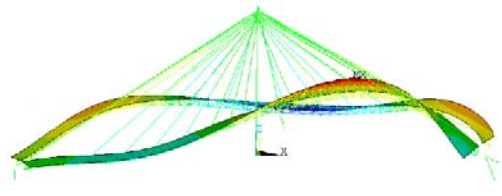

Fig. 3.4f 6th mode shape without dampers

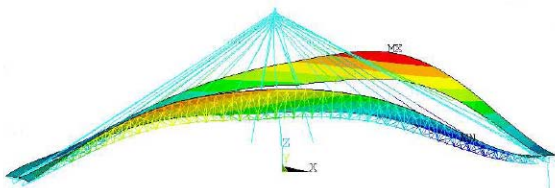

Fig. 3.4g 7th mode shape without dampers

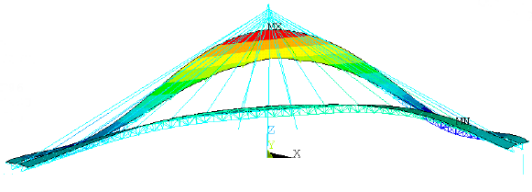

Fig. 3.4h 8th mode shape without dampers

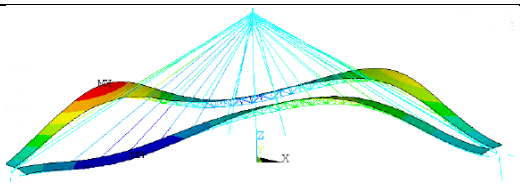

Fig. 3.4i 9th mode shape without dampers

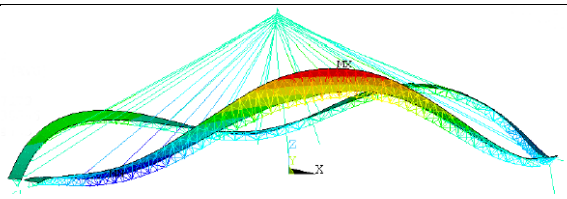

Fig. 3.4j 10th mode shape without dampers

The footbridge is subjected to mainly two types of load- wind and pedestrians. In view of the fact that wind and pedestrians loads may cause fatigue failure of the critical parts of the structure, a fatigue check was deemed necessary and was performed.

The wind load is consists of mainly three components- static, buffeting and self-excited one. By using a non-linear analysis in ANSYS, stresses in steel structural members of the bridge deck were evaluated. The values of the most stressed sections have been reported in Table 3.2.

Table 3.2: Maximal values of the most stressed structural elements

Members	Element No.	$\Delta\sigma$ [N/mm^2]	σ_{Mean} [N/mm^2]
Bottom Chord	699	12	24
External Top Chord	597	14	48
Internal Top Chord	660	25	3
Post	1052	10	19
Diagonal Members	967	12	37

In a successive phase a graphic representation of the stress history at the detail is shown in Fig. 3.5a-b for the bottom chord and the external top chord.

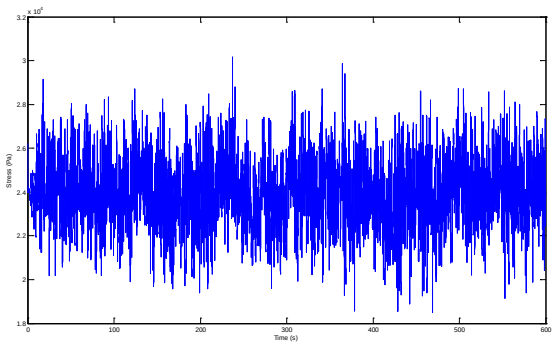

Fig. 3.5a: Stress history of the most stressed structural element of the bottom chord

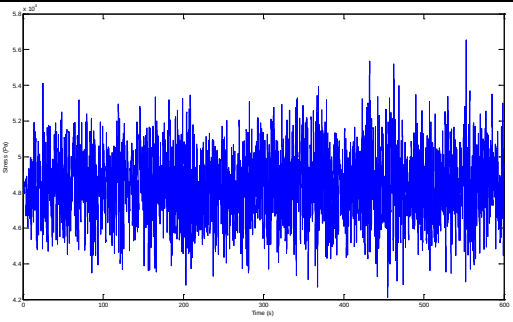

Fig. 3.5b: Stress history of the most stressed structural element of the external top chord

It was found that the deck of the 'Ponte del Mare' of Pescara has no fatigue problems due to wind actions as each one of the deck elements listed in Table 3.2 entails a stress-range value smaller than the cut-off limit.

For the fatigue check due to pedestrians loading, only modes 6 to 11 were considered. From modal analysis, the lower modes from 1 to 5, doesn't give a relevant contribution to the fatigue check because of their low value of stress range in the elements. For each mode, the load is in resonance and in phase with the mode, and acts in the same direction of the mode shape considered, for e.g. see Fig. 3.6. The dynamic part of the pedestrian load is shown in Fig. 3.7.

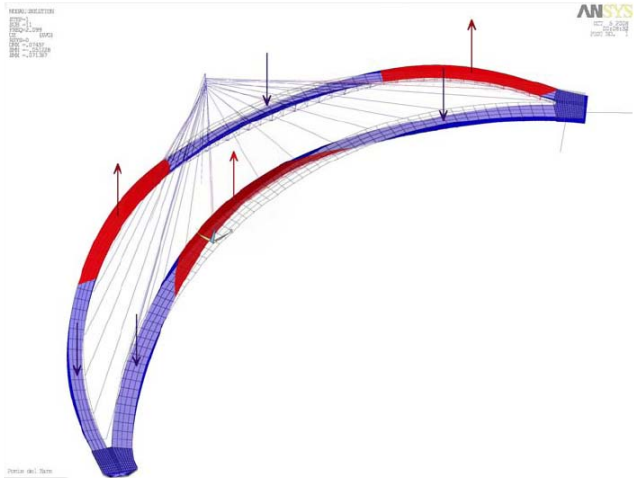

Fig. 3.6 Load model according to the mode shape of each mode

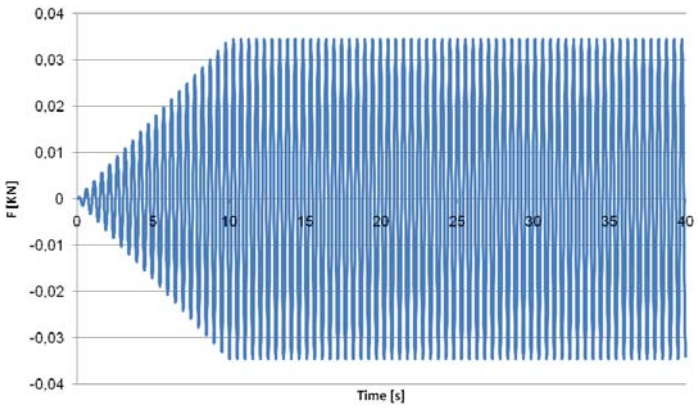

Fig. 3.7 Dynamic part of the pedestrian load

By non linear analysis in ANSYS software the stresses in the steel structural members of the bridge deck have been evaluated. For each typology of structural elements the most stressed part has been checked for fatigue. The stress ranges in the considered elements of the bridge are shown in Tables 3.3 and 3.4.

Table 3.3 Stress range in the elements due to static part of the load

MODE 5	Pedestrian deck $\Delta\sigma_{,static}$ $[N/mm^2]$	Cycling deck $\Delta\sigma_{,static}$ $[N/mm^2]$
Bottom chord	26.86	53.08
External top chord	50.59	72.41
Internal top chord	22.55	59.5
Diagonal members	77.93	77.72
Posts	77.73	77.15

Table 3.4 Stress range in the elements due to dynamic part of the load, mode 6

MODE 6	Pedestrian deck $\Delta\sigma_{,dynamic}$ $[N/mm^2]$	Cycling deck $\Delta\sigma_{,dynamic}$ $[N/mm^2]$
Bottom chord	2.90	2.24
External top chord	1.75	7.21
Internal top chord	3.12	4.27
Diagonal members	7.85	3.88
Posts	11.70	7.24

In a successive phase a graphic representation of the stress history at the detail is shown in Fig. 3.8a-b for the bottom chord and the external top chord.

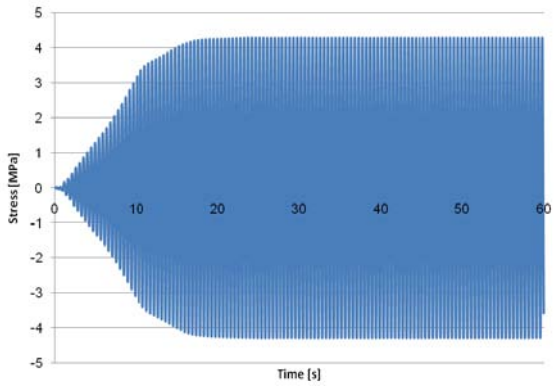

Fig. 3.8a Stress history of the most stressed structural element of bottom chord (mode 11 pedestrian deck)

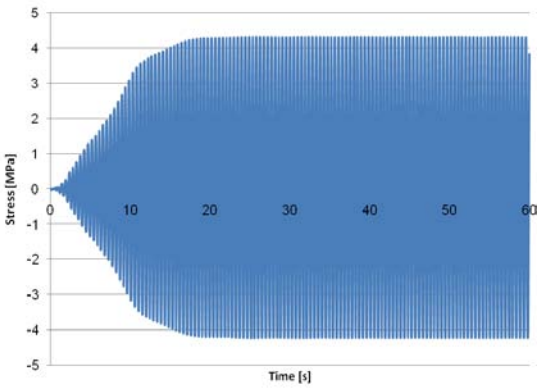

Fig. 3.8b Stress history of the most stressed structural element of external top chord (mode 11 pedestrian deck)

For normal walking, frequency may be described by a Gaussian distribution with 2 Hz average and about 0.175 Hz standard deviation. For each natural frequency is possible to define the probability of resonance and then can be calculated the number of dynamic cycles, see Fig. 3.9.

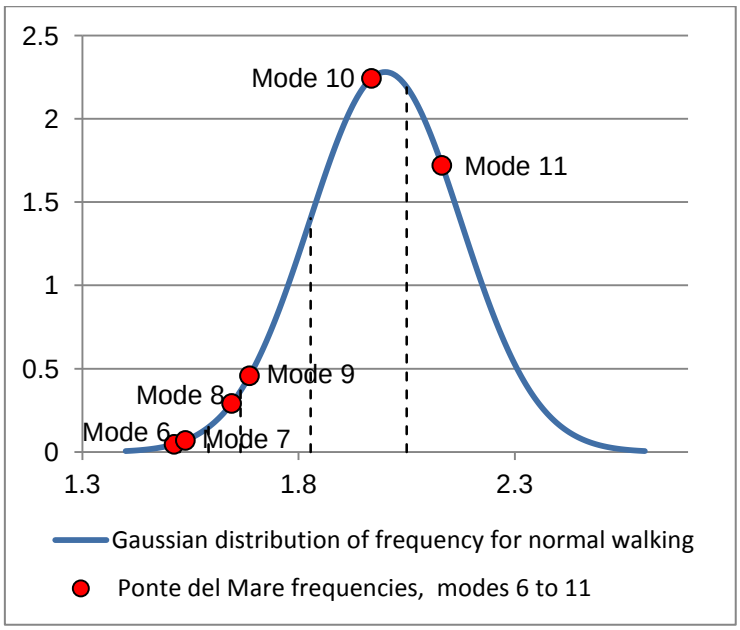

Fig. 3.9: Gaussian distribution of the frequency of human walking

The fatigue assessment has been made through damage verification according to the Palmgren-Miner formula. It was found that the deck of the 'Ponte del Mare' of Pescara has no fatigue problems due to pedestrians actions as each one of the deck elements entails a stress-range value smaller than the cut-off.

D.6.3.2 Re-design of the footbridge

The footbridge was re-designed with the circular hollow sections made of HSS TS 690 and TS 590 using SAP software. During the re-design of the bridge, the actions on the bridge structure were considered from the Eurocode 3, part 2. From the analysis it resulted that the possibility of exploitation of the High Strength Steel is remarkably limited from the problem of deformability of the structure. In summary, the employment of CHS provides the following advantages:

- More transparency of the bridge through the use of smaller sections with smaller inertia.

- Possibility to take away the hull, for aesthetic reasons, that covered the original deck of the bridge.

This should also reduce aerodynamic problems; in fact the actual footbridge is endowed with elastic-viscous-fluid dampers connected trough cables to the two decks in order to avoid flutter and galloping phenomena.

-The bridge entails a lower visual impact.

Fig. 3.10 provides a comparison between the two different type of sections.

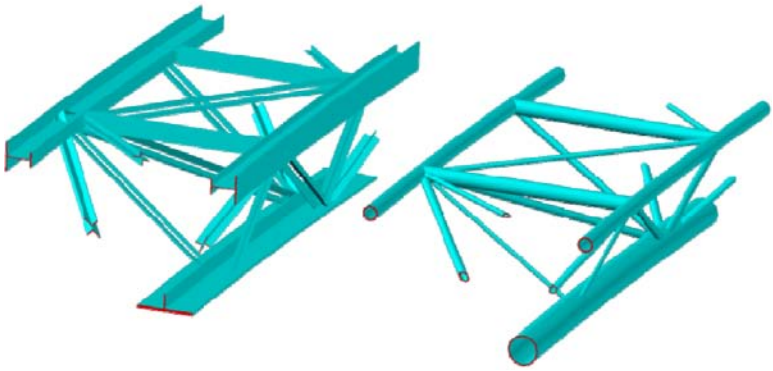

Fig. 3.10: Comparison of the deck with open and circular sections

The numerical model in SAP made of circular hollow sections is shown in Figure 3.11. The model frequencies are represented in Table 3.5. From the table, it can be observed that the modal frequency for each mode is increased in comparison to those of the open sections. Therefore, the application of CHS makes the footbridge stiffer.

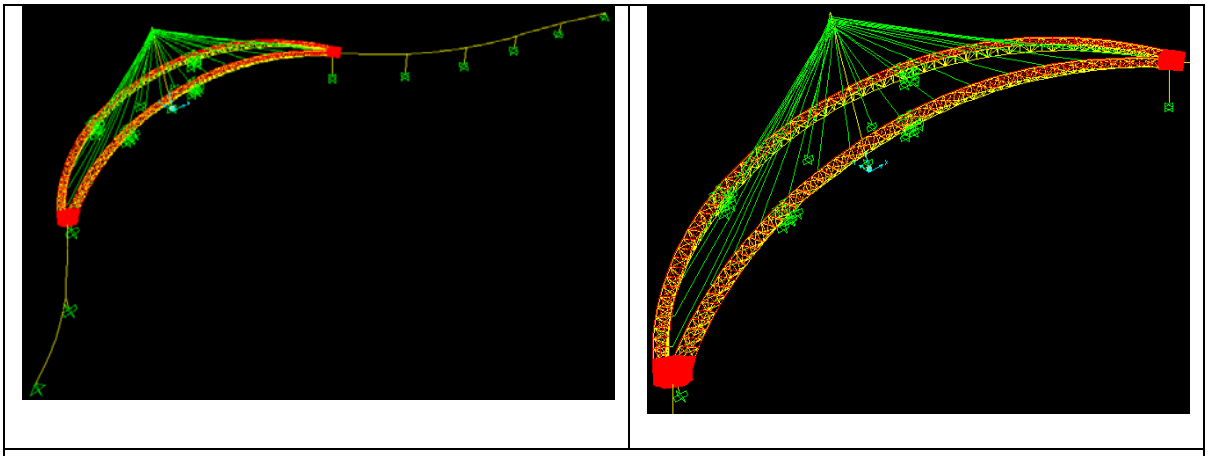

Fig. 3.11: SAP model of the footbridge with tubular sections

Table 3.5 Modal frequencies of the structure

Mode	1	2	3	4	5	6	7	8	9	10	11
f[Hz]	1.45	1.84	2.15	2.84	2.90	3.09	3.55	3.66	4.15	4.38	4.55

The frequencies from mode 1 to mode 5 are significant for the pedestrians loading as these values fall in the normal distribution range of the human walking frequency. These frequencies are embedded on a Gaussian distribution curve for the normal walking frequency of pedestrians with mean frequency =2 Hz and standard deviation = 0.175 Hz, see Fig. 3.12.

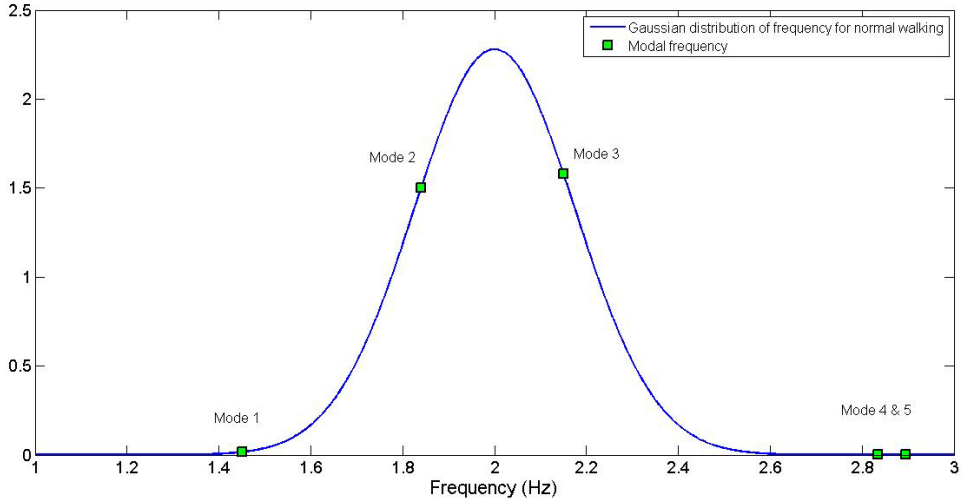

Figure 3.12: Modal frequencies shown on a Gaussian distribution plot

The types of mode shape are shown as follows:

Table 3.6: Type of modes

Mode	1	2	3	4	5
Frequency	1.45	1.84	2.15	2.84	2.90
Type	Vertical	Vertical	Vertical	Vertical	Vertical

It should be noted that the above listed mode shapes are complex, however the vibration in the vertical direction dominates. The first four mode shapes are shown in the following figures.

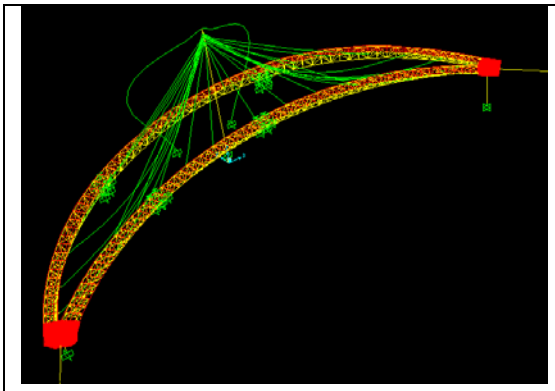

Fig. 3.13a 1st mode shape

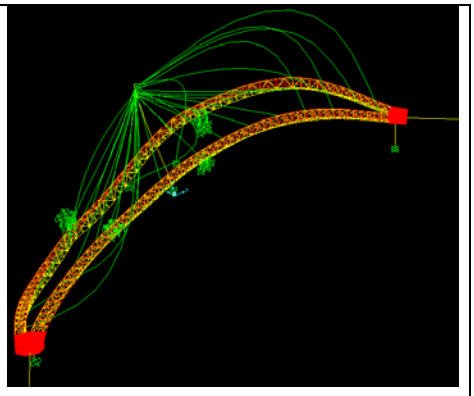

Fig. 3.13b 2nd mode shape

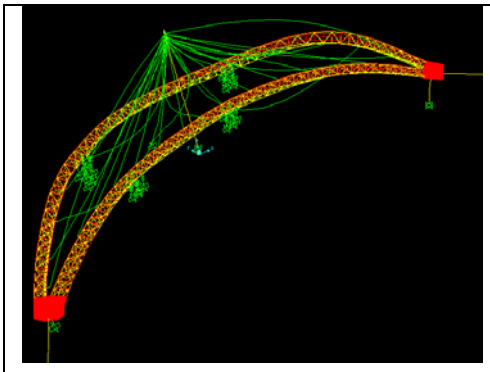

Fig. 3.13c 3rd mode shape

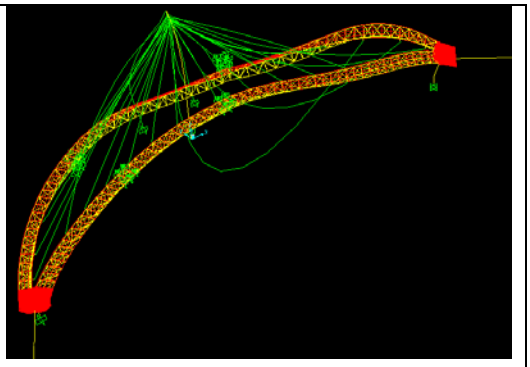

Fig. 3.13d 4th mode shape

The modal properties estimated from the modal testing campaign did not match to that of the numerical model. In order to get a robust FE model capable to simulate the actual behaviour of the footbridge, the initial FE model was updated in the light of the experimental data obtained from the identification of the bridge. The sensitivity based model updating techniques and Powell's Dog-Leg method of optimisation based on the Trust-Region approach were used. The sensitivity matrix was calculated and the 9 most sensitive parameters were selected. The final updated model showed a considerable reduction of errors relevant to frequencies. Fig. 3.14 shows the MAC values between the experimental and updated FE model.

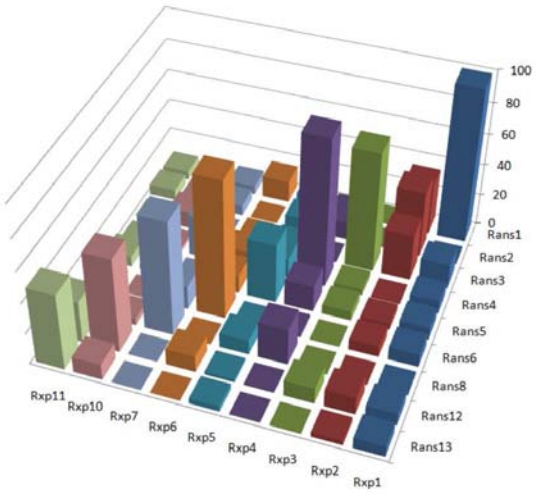

Figure 3.14,5.22: MAC, xp- experimental & ans- ANSYS

Fig. 3.15 gives a visual representation of the first updated mode shape with MAC value 98.6.

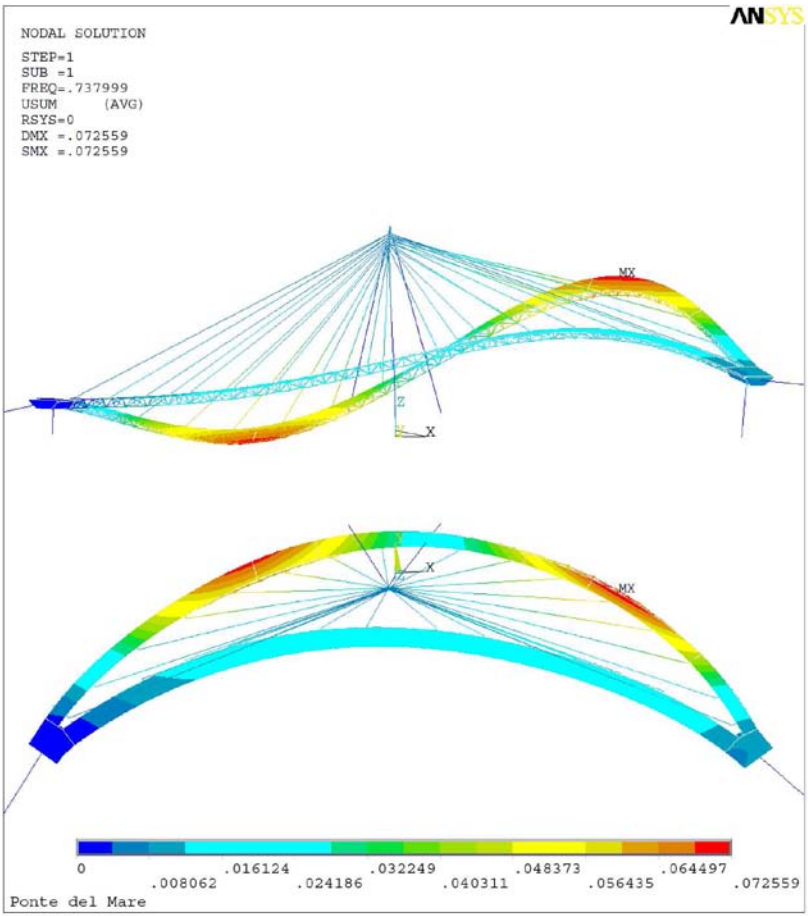

Figure 3.15: 1st mode of ANSYS correlated with 1st mode of experiment with MAC=98.6

After the updating of the FE model with the 9 parameters, the same was considered to use to reproduce the acceleration response under the actual wind loading to check the applicability of the model. The 'Ponte del mare' bridge is under monitoring with 8 accelerometers since December 2009. An especially intense wind recorded on 25/12/2009 during 12:49 - 12:59 was chosen for the simulation.

The mean wind speed near the deck was considered 16.19 m/s, i.e. an average of the measurement obtained from the two anemometers one below the deck and other on the top of the mast.

Figures 3.16a and 3.16b present the acceleration response obtained after the execution of the analysis on the model without the dampers while that with the connected dampers is shown in Figures 3.16c and 3.16d. It can be noticed that the trend of the accelerations and the maximum values for the node corresponding to the accelerometer M1 are approachable to the records of the same accelerometer.

This behavior, as appears good, is checked also for the M5, nevertheless, that happens mainly because the values of acceleration in M1 and M5 are very low because they are positioned in the proximity of the ramp of access to the deck. In fact, all the other comparisons are like that of M3 in Figure 3.16d and to check simply the order of magnitude by calculating the root-mean-square (RMS) values presents large percentage difference.

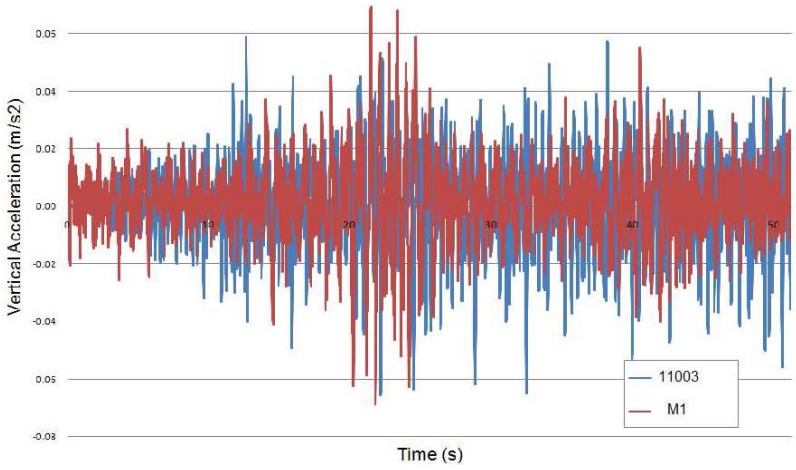

Figure 3.16a: comparison between the acceleration recorded at M1 with the vertical acceleration at node 11003 of ANSYS model without dampers

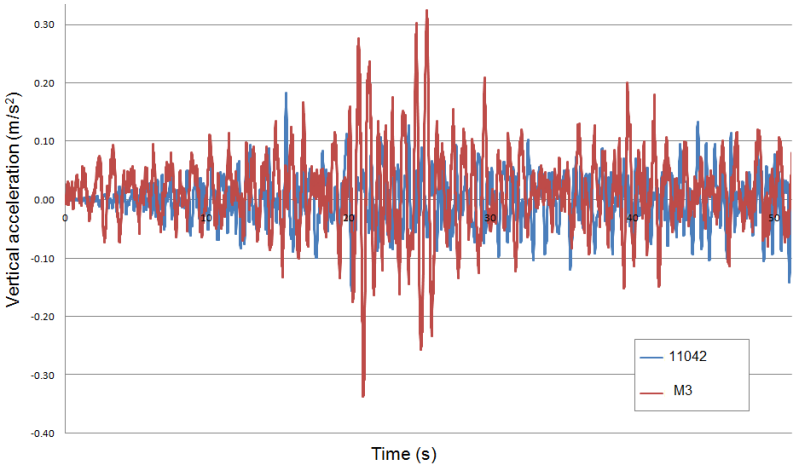

Figure 3.16b: comparison between the acceleration recorded at M3 with the vertical acceleration at node 11042 of ANSYS model without dampers

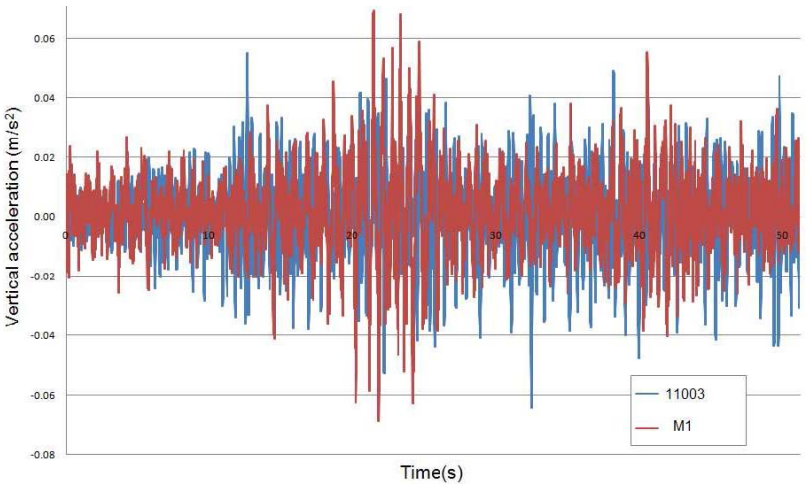

Figure 3.16c: comparison between the acceleration recorded at M1 with the vertical acceleration at node 11003 of ANSYS model with dampers

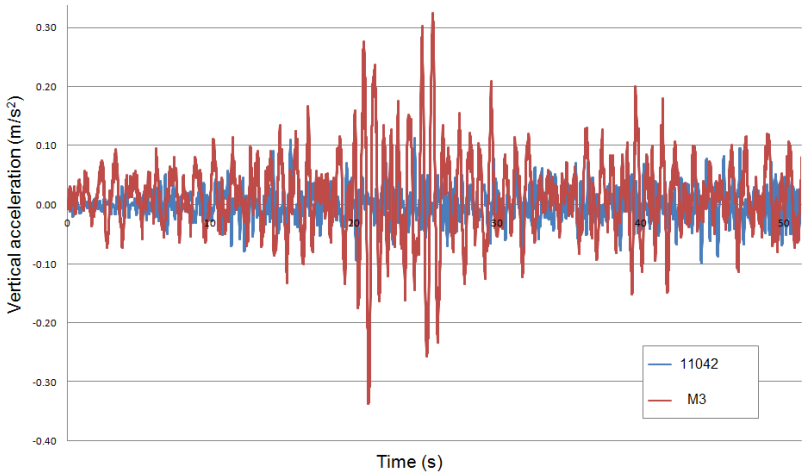

Figure 3.16d: comparison between the acceleration recorded at M3 with the vertical acceleration at node 11042 of ANSYS model with dampers

The updated model well reproduced the response of the footbridge under an actual wind loading condition characterized by an average velocity of 16.19 m/s. Moreover and in the case of dampers, it underestimated the acceleration response with respect to the one obtained from measurements. This was due to the fact that, in reality, dampers are characterized by slack up to displacements of 4 mm.

D.6.3.3 S. Michele footbridge

S. Michele footbridge is situated in the town of San Michele in the province of Trento, Italy, see Figure 3.17. For the modal analysis the footbridge was modeled in ANSYS software and the modal frequencies and mode shapes were estimated.

Figure 3.17: Footbridge 'S. Michele' under construction

For the fatigue check modes 2 to 8 were considered as these frequencies fall in the human walking range. For each mode, the load is in resonance and in phase with the mode, and acts in the same direction of the mode shape considered.

The natural frequencies of the modes considered are given in Table 3.7.

Table 3.7 Natural frequencies of modes 2 to 8 of S. Michele

Mode	2	3	4	5	6	7	8
f [Hz]	0.6704 (lateral)	0.7178 (lateral)	0.8823 (lateral)	1.0676 (lateral)	1.3377 (vertical)	1.9322 (vertical)	2.0038 (vertical)

The FE model and some mode shapes are shown in the following figures 3.18-3.19.

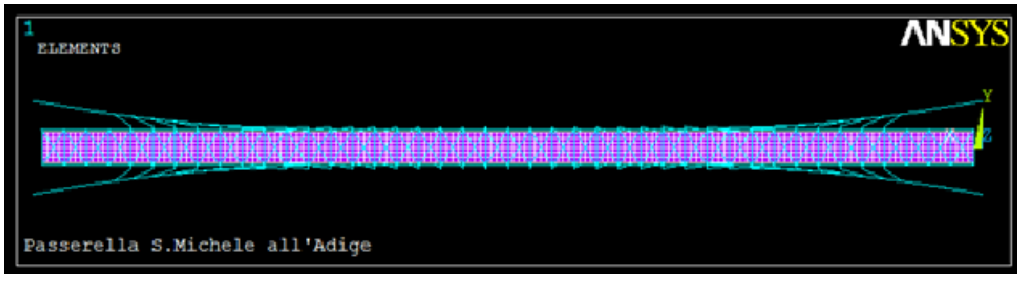

Figure 3.18: Finite element model of the 'S. Michele' footbridge in ANSYS

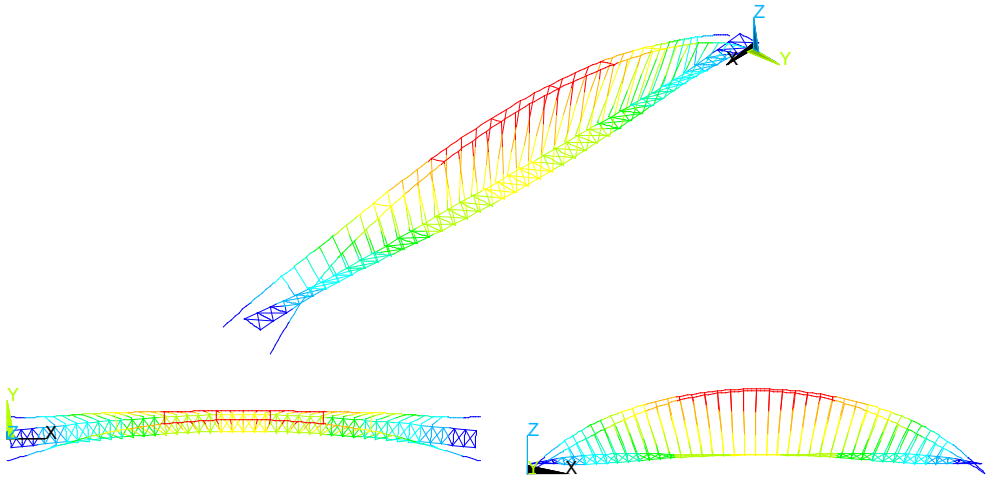

Figure 3.19a: Mode shape 2, f= 0.6704 Hz

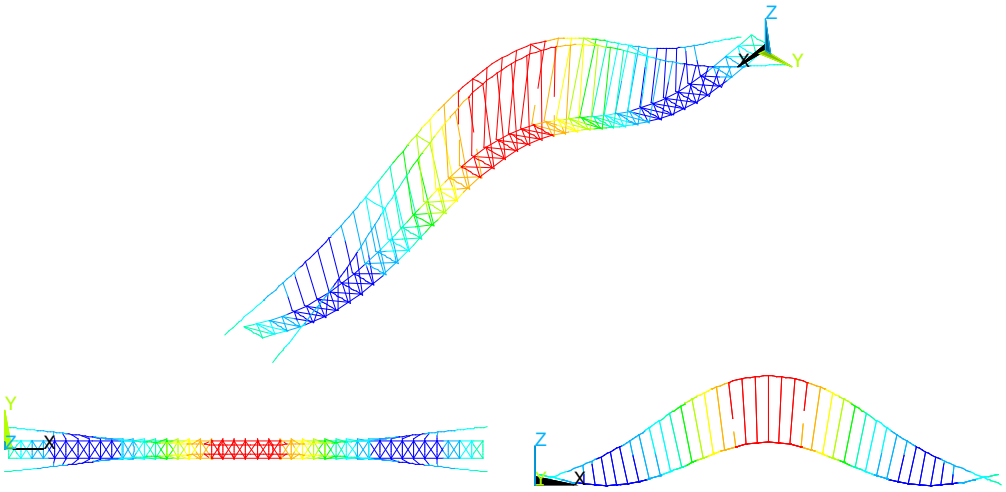

Figure 3.19b: Mode shape 5, f= 1.0676Hz

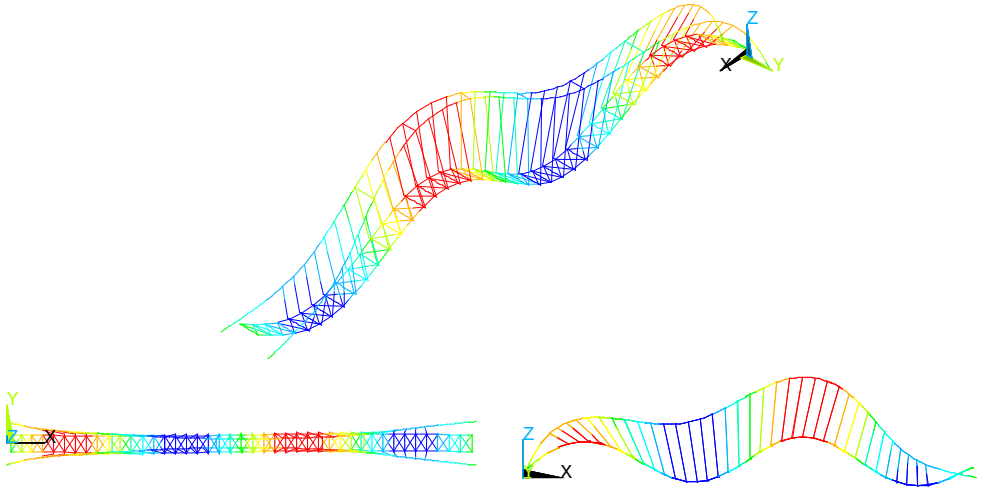

Figure 3.19c: Mode shape 8, f= 2.0038Hz

In a successive phase a graphic representation of the stress history at the detail is shown in Fig. 3.20 for the chord-chord welded joint.

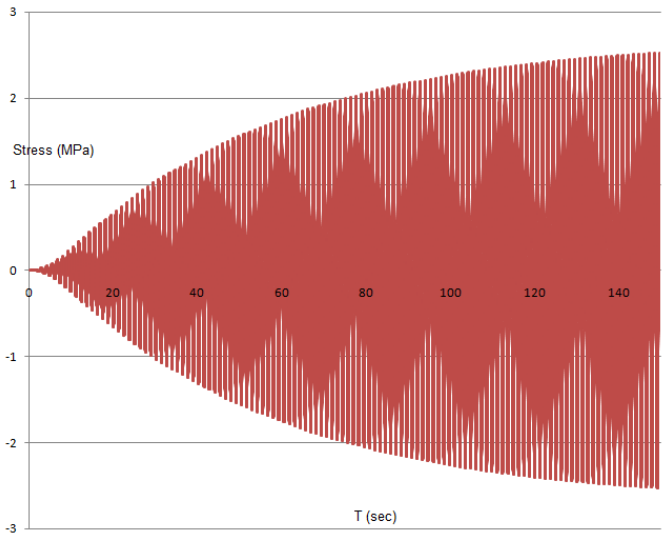

Figure 3.20: Stress history of the chord-chord welded joint Mode 2 (Element number 346)

For normal walking, frequency may be described by a Gaussian distribution with 2 Hz average and about 0.175 Hz standard deviation. For each natural frequency is possible to define the probability of resonance and then can be calculated the number of dynamic cycles, see Figure 3.21.

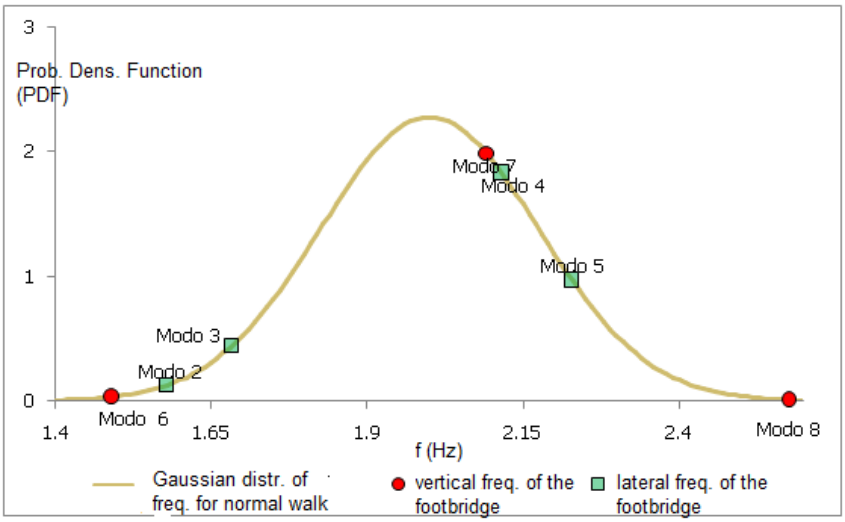

Figure 3.21: Gaussian distribution of the frequency of human walking

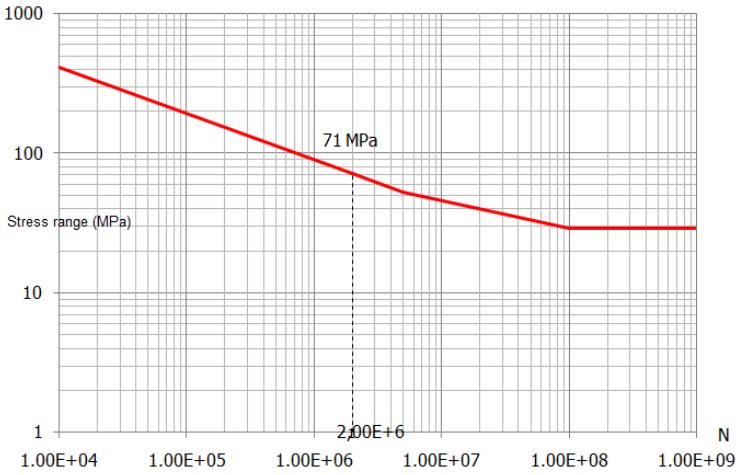

Figure 3.22: Stress range and number of cycles for mode 2, element number EN 245, EN 001 /A

Table 3.8 presents the stress-ranges calculated from the above curve for each detail.

Table A6.8: Stress ranges for the details		
Element number	$\Delta\sigma_c$ (MPa)	$\Delta\sigma_L$ (MPa)
EN245	71	28.73
EN346	63	25.50
EN001/A	71	28.73
EN001/B	50	20.24
EN001/C	100 (m=5)	25.12
EN449/A	50	20.24
EN449/B	100 (m=5)	25.12

It was found that stress ranges are below the cut-off, i.e. $\Delta\sigma<\Delta\sigma_L$. Henec, they do not give a contribution to the damage of the considered details.

Therefore, the elements of the “S. Michele” footbridge in Trento are safe with respect to the pedestrians fatigue loading.

D.6.3.4 Nomi footbridge

Nomi footbridge is situated in the town of Nomi in the province of Trento, Italy, see Figure 3.23. For the modal analysis the footbridge was modeled in ANSYS software and the modal frequencies and mode shapes were estimated.

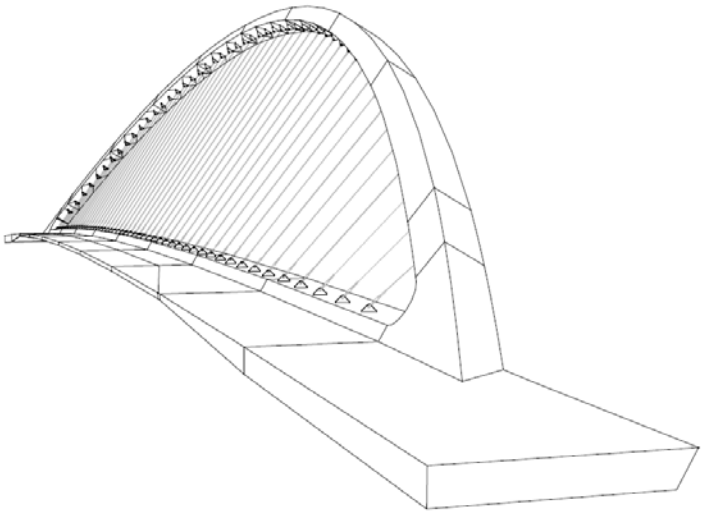

Figure 3.23: Design view of the “Nomi” footbridge.

The modal shapes of the “Nomi” footbridge considered are shown in Figure 3.24.

(a)

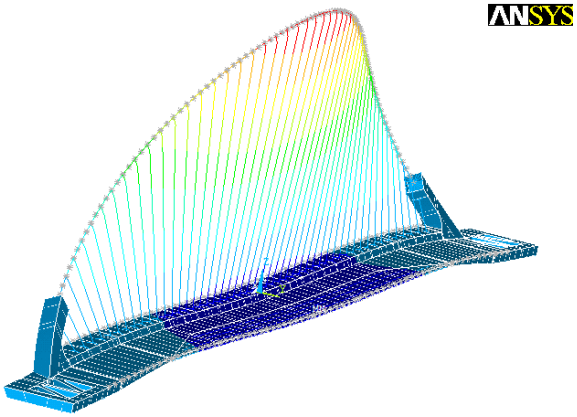

(b)

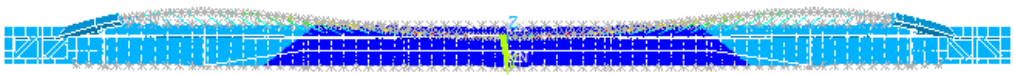

(c)

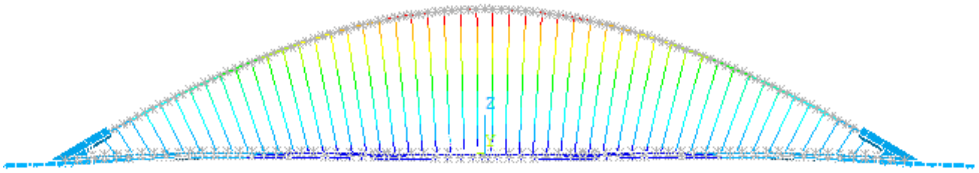

Figure 3.24a: Mode shape 1; three-dimensional (a), top (b) and longitudinal (c) view.

(a)

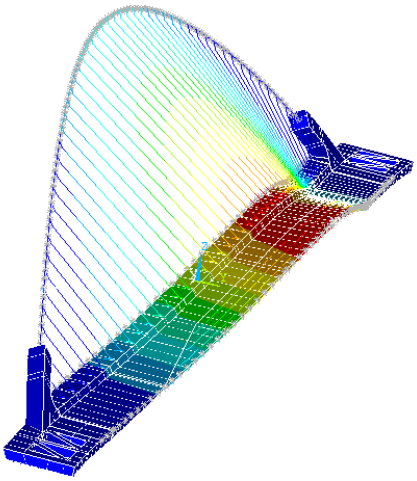

(b)

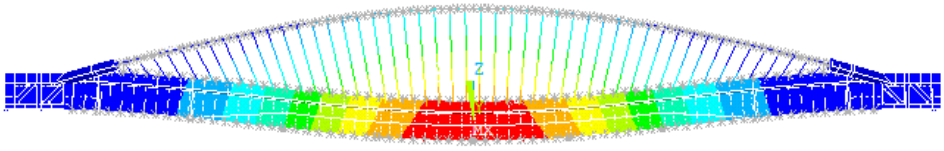

(c)

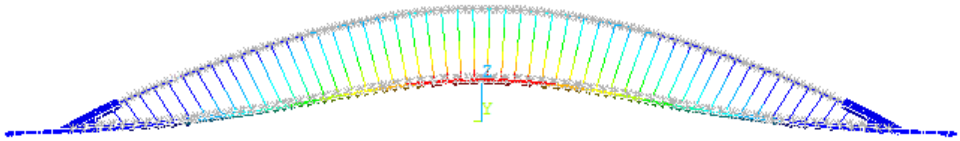

Figure 3.24b: Mode shape 2; three-dimensional (a), top (b) and longitudinal (c) view.

(a)

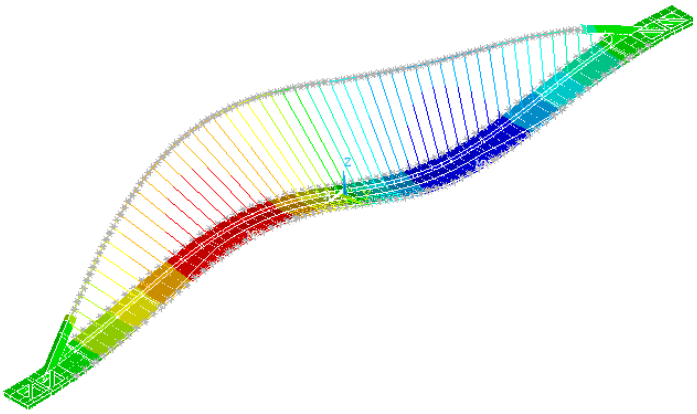

(b)

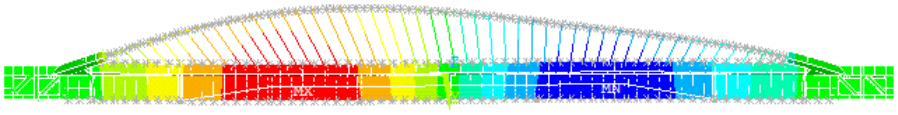

(c)

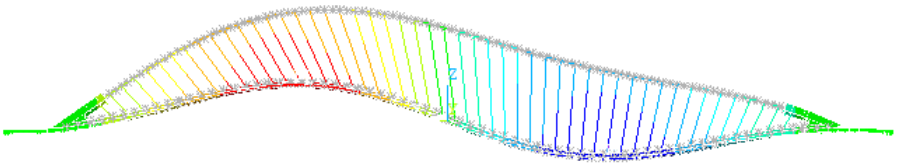

Figure 3.24c: Mode shape 3; three-dimensional (a), top (b) and longitudinal (c) view.

(a)

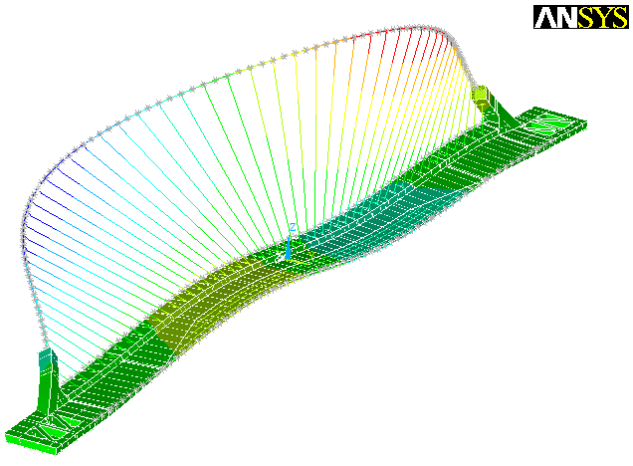

(b)

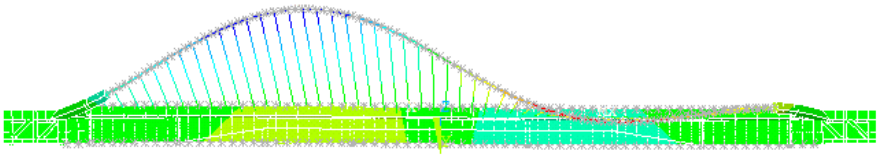

(c)

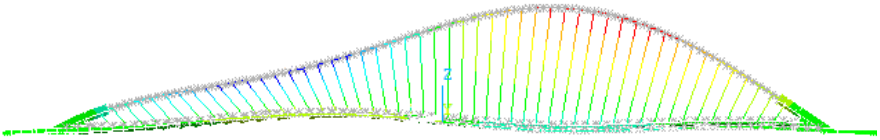

Figure 3.24d: Mode shape 4; three-dimensional (a), top (b) and longitudinal (c) view.

(a)

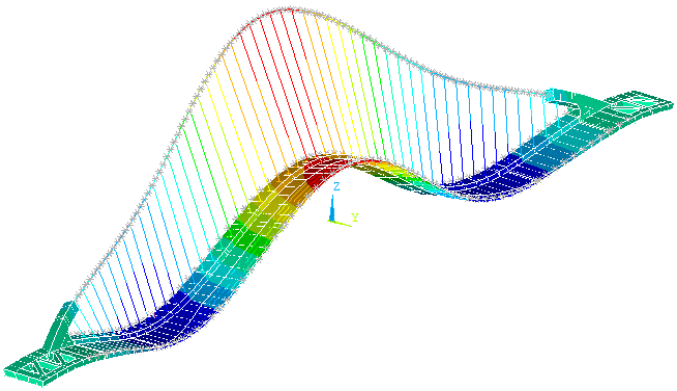

(b)

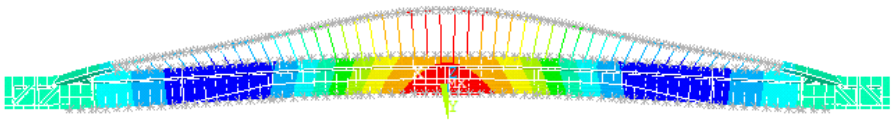

(c)

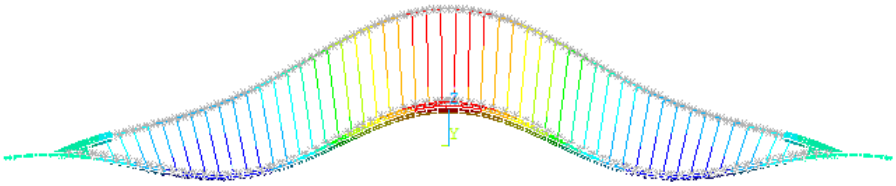

Figure 3.24e: Mode shape 5; three-dimensional (a), top (b) and longitudinal (c) view.

For the fatigue check modes 1 to 5 are considered as these frequencies fall in the human walking range. For each mode, the load is in resonance and in phase with the mode, and acts in the same direction of the mode shape considered. The natural frequencies of the modes considered are given in Table 3.9.

Table 3.9: Natural frequencies of modes 1 to 5 of “Nomi” footbridge

Mode	1	2	3	4	5
f [Hz]	0.73936 (lateral arch)	1.21354 (lateral-vertical)	1.21586 (vertical)	1.87616 (lateral-vertical arch)	2.17270 (vertical)

A typical stress history in a welded detail under pedestrians loading is shown in Figure 3.25.

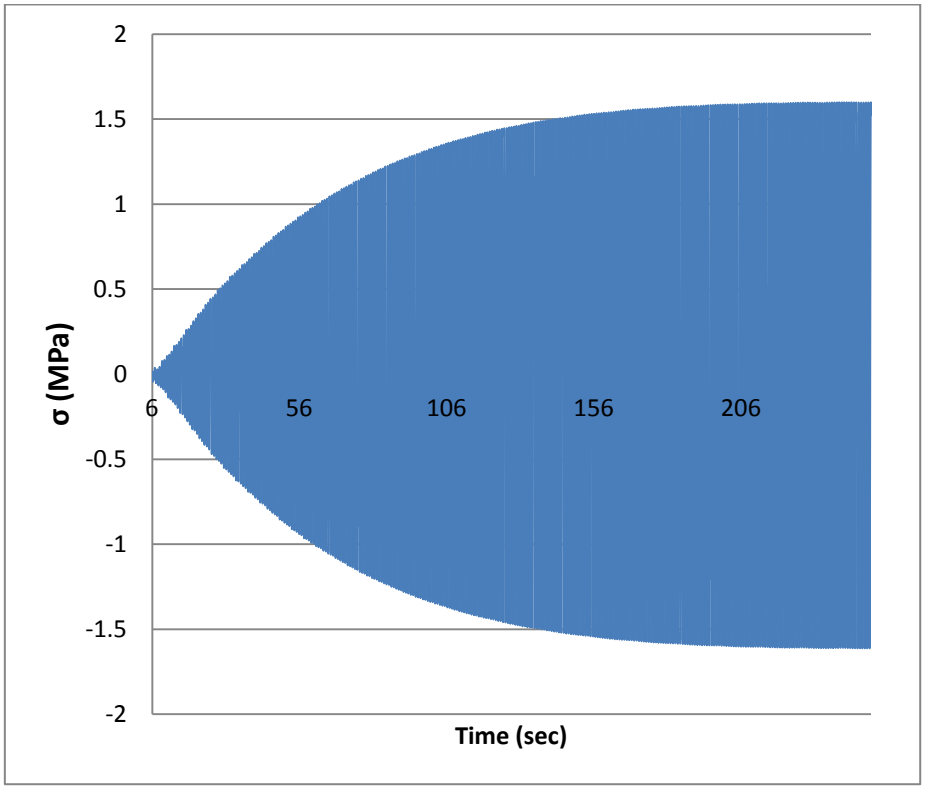

Figure 3.25: Stress history of the arch-arch welded joint Mode 2VH (EN 982)

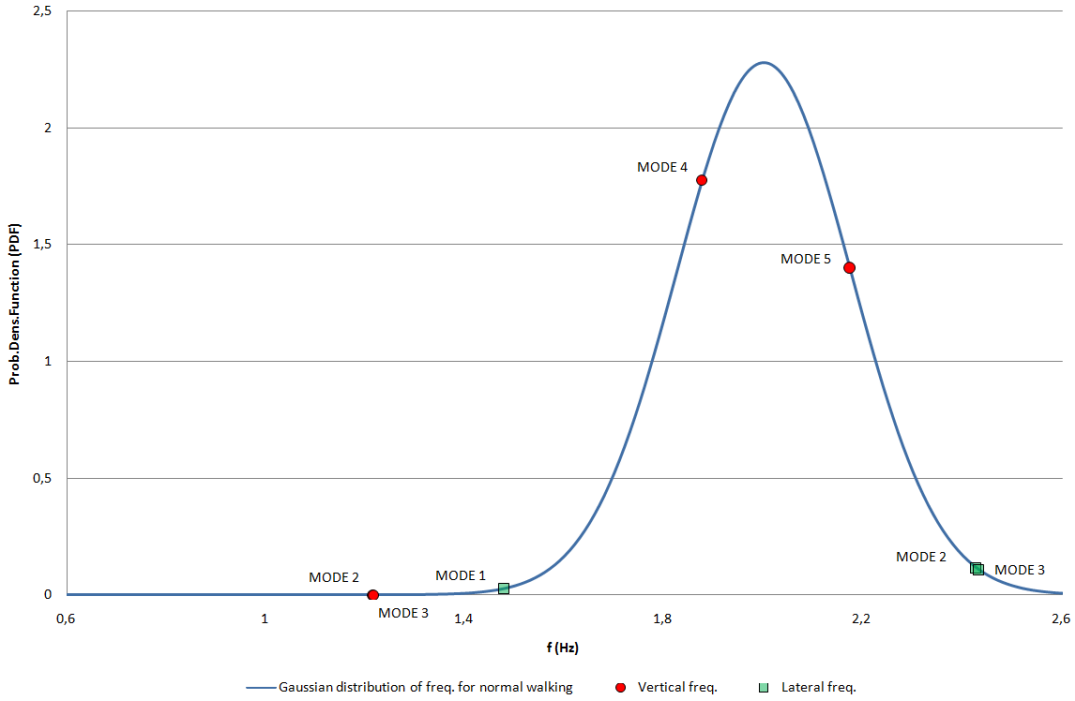

Figure 3.26: Gaussian distribution of the frequency of human walking

All stress ranges for arch details show that $\Delta\sigma_E < \Delta\sigma_L$, so they do not give a relevant contribution to the damage of details.

D.6.3.5 Conclusions

The simulations were performed on three case studies, i.e. Ponte del Mare of Pescara, S. Michele and Nomi footbridges, respectively. In detail, Ponte del Mare footbridge was modelled in ANSYS software then updated based on the experimental data and used to simulate the actual wind loading. The same footbridge was re-designed using circular hollow sections made of high strength steels. It was found that the natural frequencies increased and the bridge became stiffer. The fatigue checks were performed on all the three case studies and none of the footbridge was prone to fatigue problems owing to pedestrians. Therefore, we can conclude that footbridges don't exhibit fatigue problems due to pedestrians loading.